



# Validation of Foreground Emission Model using GALEX Medium Observations

Nimmi Narayanan<sup>1,2</sup>, Shivashankar S. Menon<sup>3</sup> , and N. V. Sujatha<sup>1</sup>

<sup>1</sup> Department of Physics, St. Xavier's College for Women, Aluva 683101, India; [sujathanv@stxaviersaluva.ac.in](mailto:sujathanv@stxaviersaluva.ac.in)

<sup>2</sup> Department of Physics, Sree Sankara College, Kalady, Ernakulam 683574, India; [nimmi.indhira@gmail.com](mailto:nimmi.indhira@gmail.com)

<sup>3</sup> CSIS, BITS Pilani K. K. Birla Goa Campus, Zuarinagar, Goa 403726, India; [f20190034@goa.bits-pilani.ac.in](mailto:f20190034@goa.bits-pilani.ac.in)

Received 2022 September 29; revised 2023 April 9; accepted 2023 April 13; published 2023 May 30

## Abstract

The study of diffuse ultraviolet (UV) background radiation is vital in the investigation of stellar and galactic evolution. Space-based UV observations are comprised of both foreground and background radiations. The foreground emission in an observation is a result of solar contamination in the direction of observation. In our previous work, we modeled airglow (one of the major constituents of the foreground emission) as a function of 10.7 cm Solar Flux and Sun Angle with great accuracy using GALEX deep observations. We adopt a similar methodology to validate the obtained model and run equivalent experiments here using far-UV (FUV) and near-UV (NUV) GALEX medium imaging surveys (MIS) with a total exposure time greater than 3300 s. We obtained a predictive model having excellent compatibility with the earlier model. Our analysis shows that the total foreground emission varies between 59 and 295 photon units in FUV whereas in NUV, it varies between 671 and 1195 photon units depending upon the date and time of observation. We also noticed a strong correlation between the background emission and optical depth both in FUV and NUV, especially in the low density regions. This clearly indicates that the major contributor in diffuse background radiation is the starlight scattered by interstellar dust grains.

**Key words:** instrumentation: detectors – Sun: activity – ultraviolet: ISM – atmospheric effects

## 1. Introduction

Our understanding of diffuse ultraviolet (UV) radiation since 1991 (Bowyer 1991; Henry 1991; Murthy 2009) has improved with advancements in instrument sensitivity in the past decade. With state-of-the-art space telescopes providing high-quality data, there has been a push toward obtaining a better understanding of UV and infrared (IR) radiation—comprising a component that absorbs stellar UV radiation and re-emits it at longer wavelengths—to unravel the structure and characteristics of interstellar dust and gas. This is motivated by space-based UV radiation being a combination of foreground emission and background radiation. This makes proper extraction and removal of the foreground emission component essential for retrieving information about background radiation, which is made up of astrophysical signals like atomic and molecular emission, dust-scattered starlight, and any other extra-galactic contribution. However, owing to its diffuse nature and low brightness, the determination and analysis of UV radiation are both tedious and vague.

With the availability of improved instrumentation techniques and better resolution, researchers have been able to make remarkable advancements in this field. Sujatha et al. (2009) and Sujatha et al. (2010) modeled foreground emissions using Deep Imaging Surveys (DIS) of a region of nebulosity first observed

by Sandage in 1976 and the Draco constellation, respectively. Murthy (2014a) developed sky background images in near-UV (NUV) and far-UV (FUV) bands using Galaxy Evolution Explorer (GALEX, a space telescope launched by NASA in 2003). They used a GALEX field-of-view of only  $1^{\circ}1$  in their analysis to avoid edge effects. Murthy (2014b) derived an empirical model for airglow and zodiacal light foreground emissions as a function of Sun Angle (SA) using all-sky GALEX surveys. As Narayanan et al. (2023) however later showed, a deeper analysis of deep GALEX observations revealed an additional dependence of solar flux in these emissions, and we accordingly developed a multivariate empirical model for airglow from DIS observation tiles using machine learning techniques.

In this work, we conduct further tests of robustness on the multivariate model by letting the model ensemble train on GALEX Medium Imaging Surveys (MIS) observations using the same procedure described in our previous work, and checking if the new model thus obtained is within the permitted error margins of the previous model (Narayanan et al. 2023).

### 1.1. Observation Details

GALEX—an orbiting UV telescope deployed at an altitude of 600 km with a revolution period of 90 minutes—collected

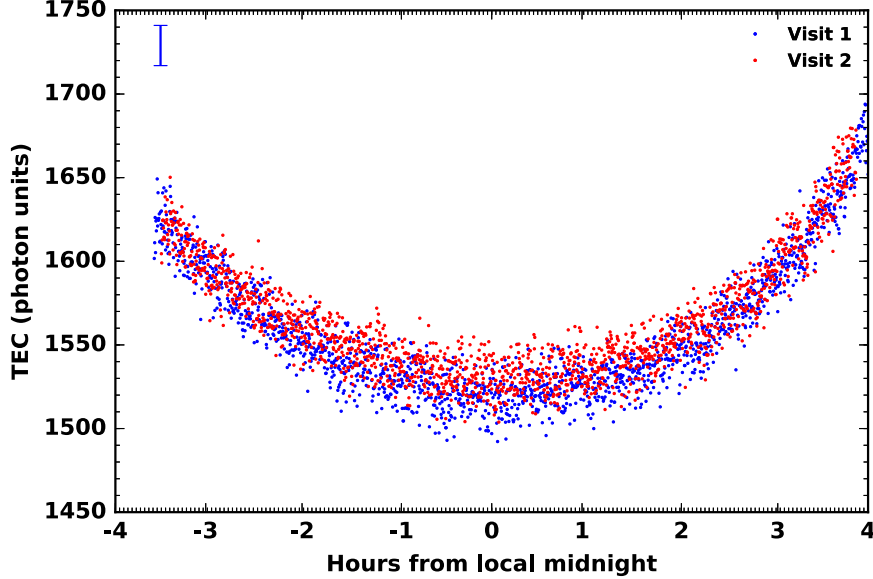


**Figure 1.** Variation of TEC (in photon units) about the local midnight of observation visits in MIS TILE MISDR1\_18032\_0666. The TEC value at local midnight (TECMIN) corresponds to the minimum value of this bell curve. Inset in the top left corner is a representative error bar corresponding to the root mean square (rms) error equalling  $\pm 12$  photon units.

light in two UV bands, namely FUV: 1350–1750 Å and NUV: 1750–2850 Å with the help of a dichroic mirror. GALEX conducted night surveys, namely All-sky Imaging Surveys (AIS), MIS and DIS with varying area and time of observations (Martin et al. 2005; Morrissey et al. 2007). Even though there are 6964 MIS observations in the latest GR6/GR7 release within the GALEX-MAST archive, the number of observations in FUV and NUV bands with an exposure time of  $\sim 3000$  s is limited to only two or three visits for the majority of observations. To reduce model errors induced by poor-quality data, the experiments in this work only use observations with exposure time greater than 3300 s in both FUV and NUV.

A better understanding of background radiation is possible only if the contamination from the Sun—in essence, foreground emissions—is removed. Earlier in Narayanan et al. (2023), we successfully modeled foreground emissions (especially, airglow) for deep observations (DIS) as an empirical multivariate function of solar activity and SA. Airglow corresponds to resonantly scattered OI lines at 1356 Å and 2471 Å, contributing to about 200–300 photons  $\text{cm}^{-2} \text{s}^{-1} \text{sr}^{-1}$  Å $^{-1}$  (referred to hereafter as photon units) to both bands (Boffi et al. 2007). Airglow in the “look” direction (i.e., line-of-sight of the telescope during an observation) can be quantified from the variation of the spacecraft’s Telemetered Event Counter (TEC) with respect to the orbital time of the telescope. Here TEC refers to the total number of UV photons per second in both bands (Figure 1), and includes the diffuse UV background along with other contaminants (Narayanan et al. 2023). House-keeping files like the “Spacecraft State” (.scst) files keep a

record of TEC values with orbital time. Zodiacal light is considered negligible in FUV, and is determined as a function of helio-ecliptic coordinates in NUV based on a lookup table developed by Sujatha et al. (2009) using Leinert et al. (1998).

## 2. Airglow Modeling

Airglow can be extracted from the zodiacal-light-subtracted TEC values in NUV and the TEC values themselves in FUV. The baseline values (hereafter referred to as “TECMIN”) correspond to the TEC value at local midnight in either band. The strong linear correlation found between the FUV and NUV TECMINS of corresponding MIS observations (Figure 2) reveals the common sources of contaminants in the radiation. The error bars depicted in the figure correspond to the rms error values of the scatter in data with respect to the best-fit bell curve on both axes. From the in-depth analysis previously conducted in Narayanan et al. (2023), we found out that the airglow at any target location is made up of two components. The first component is a “baseline” airglow we termed AG<sub>c</sub> that varies with changes in solar activity and the geometric angle between the Sun and the target location at the time of observation (which we named the “Sun angle”). The second component is a “variable” airglow we named AG<sub>v</sub> that is a strong function of local time and symmetric about the local midnight. We call this component “variable” as it changes during a single observation according to the local time. In contrast, the former component does not change over the course of a single observation and can be thought of as a “baseline” part dependent only on the target location, solar

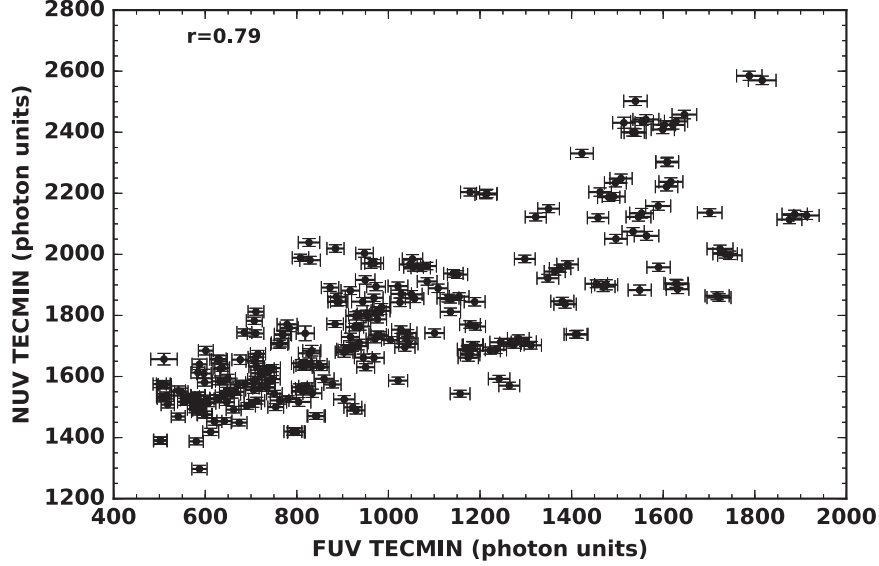


**Figure 2.** NUV TECMIN is plotted against FUV TECMIN of MIS observations. Lack of tight correlation is mainly due to the contamination of zodiacal light in the NUV.

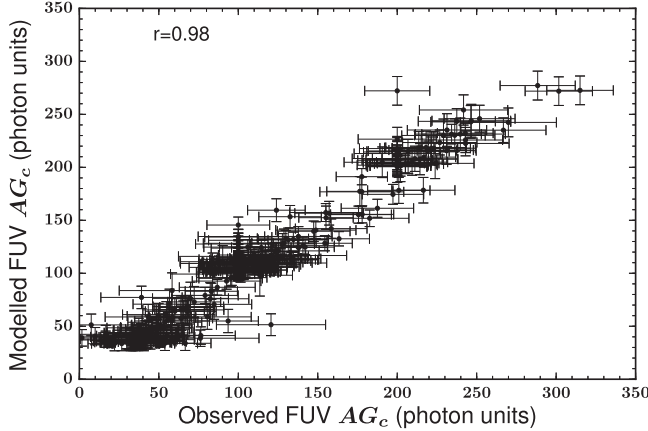


**Figure 3.** High correlation between observed and modeled  $AG_c$  in FUV within  $1\sigma$  error for model parameter  $b$  given in Table 1.

activity and the geometric SA, and independent of the local time during the observation interval.

### 2.1. Baseline Airglow ( $AG_c$ )

The baseline airglow component corresponds to the minimum values (TECMIN) of bell curves, which we found to be highly dependent on the Solar Flux (SF) and SA at the time of observation. We obtain the value for the 10.7 cm SF at the Earth in SF units ( $1 \text{ sfu} = 10^{-22} \text{ Wm}^{-2} \text{ Hz}^{-1}$ ) during each observation from the Canadian Space Weather Solar Monitoring program (Chatterjee & Das 1995). The SA being referred to here corresponds to the geometric angle between the Sun and the target of observation. The detailed analysis of DIS

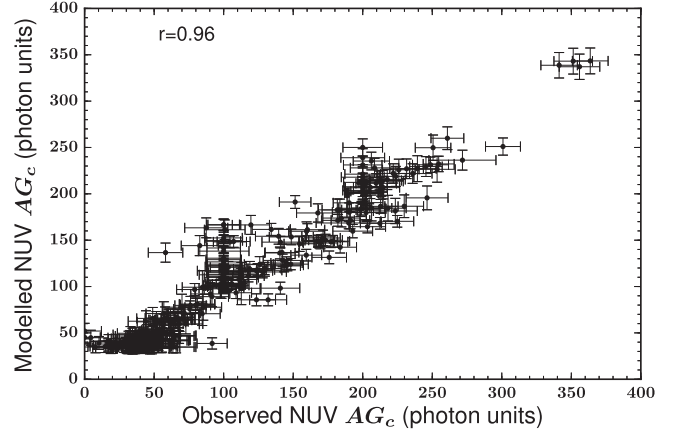


**Figure 4.** High correlation between observed and modeled  $AG_c$  in NUV within  $1\sigma$  error for model parameter  $b$  given in Table 1.

observation visits we conducted showed that  $AG_c$  is a strong function of SF and SA (Narayanan et al. 2023) according to the empirical equations

$$\text{TECMIN} = a + AG_c, \quad (1)$$

where  $a$  corresponds to the background sky radiation, and

$$AG_c = b \cdot \frac{\text{SF}}{\sin^3\left(\frac{\text{SA}}{2}\right)}, \quad (2)$$

where  $b$  corresponds to the scaling factor with most of its values lying in the interval [0.5, 2.5]. In concrete terms, this scaling factor is a measure of how strongly the “baseline”

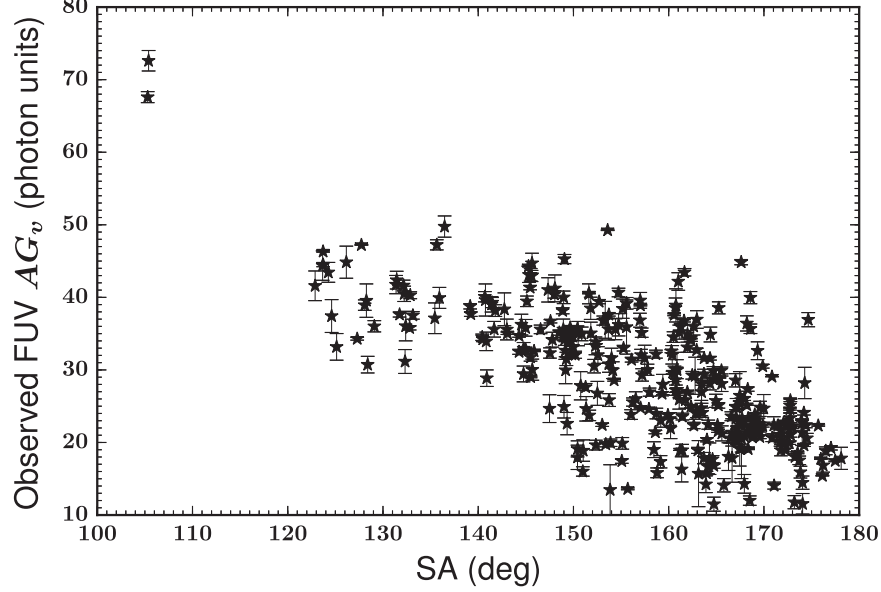


**Figure 5.** Negative correlation between observed  $AG_v$  and SA in FUV visits. The error bars correspond to variations in the area on fitting curves at extreme points.

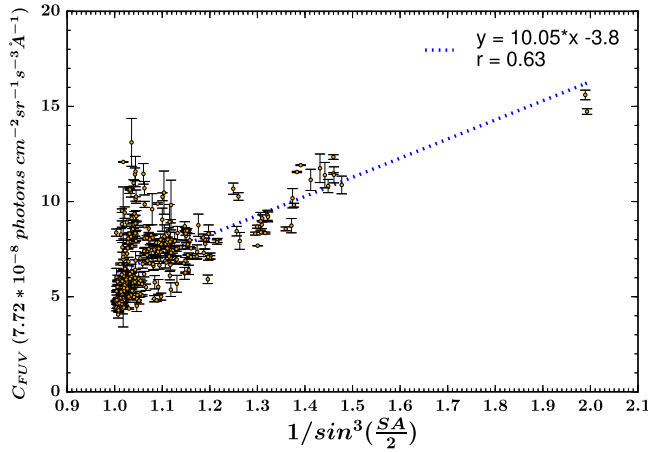


**Figure 6.** Linear correlation in the scatter plot between  $C_{\text{FUV}}$  and  $1/\sin^3\left(\frac{\text{SA}}{2}\right)$ .

airglow depends on the SF and SA at the date and time of observation. Since we know the values of TECMIN, SF and SA at the date and time of the observation, the problem of modeling reduces to a simpler task of finding the right coefficients for our  $y = a + bx$  equation, where  $y$  stands for TECMIN and  $x$  stands for the combined solar expression  $\frac{\text{SF}}{\sin^3(\text{SA}/2)}$ .

As mentioned before, since  $b$  is a scaling factor that is a measure of how “important” the above-mentioned solar expression is to determine the “baseline” airglow, it would be reasonable to obtain a singular  $b$  value across all target locations, which would result in differing  $a$  values for each

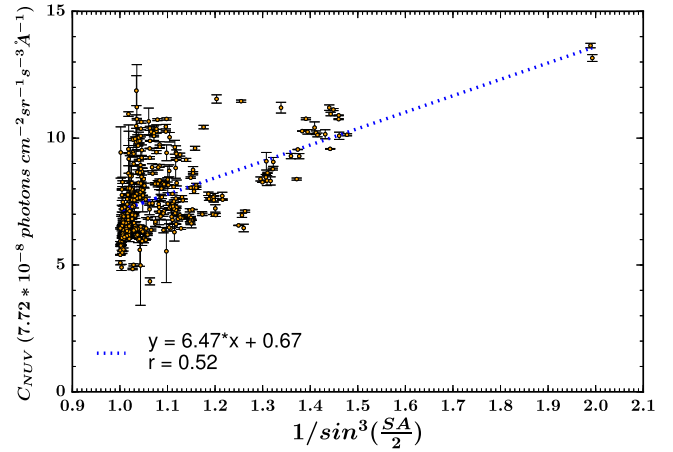


**Figure 7.** Linear correlation in the scatter plot between  $C_{\text{NUV}}$  and  $1/\sin^3\left(\frac{\text{SA}}{2}\right)$ .

target location. This would also come within our expectations for this model, as  $a$  stands for the background sky radiation and would understandably change as the telescope looks at different parts of the night sky. If these hypotheses for  $a$  and  $b$  are correct, then we should be able to obtain a model with a single  $b$  value across all visits and target locations and one  $a$  value for each target location, that lets the model estimate TECMIN within acceptable error margins when given only the values of SF and SA.

Using a chi-square minimization procedure by varying the parameter  $b$  in range [0.5, 2.5] with a coarse step-size of 0.01, we found that  $b$  can be fixed at 1.23 in FUV and 1.18 in NUV with a reduced chi-square of 0.15 and 0.32

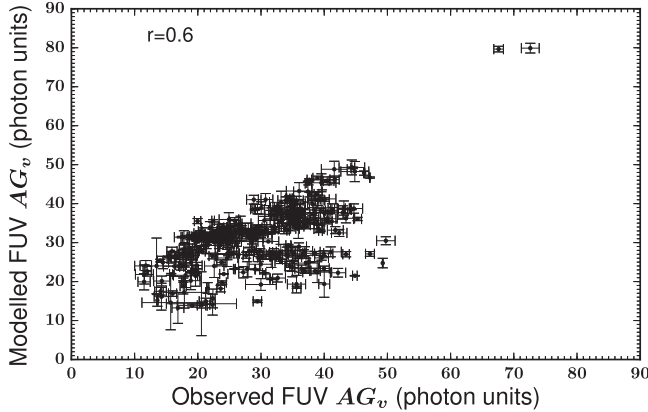


**Figure 8.** Correlation in the scatter plot between observed and modeled AG<sub>v</sub> in FUV.

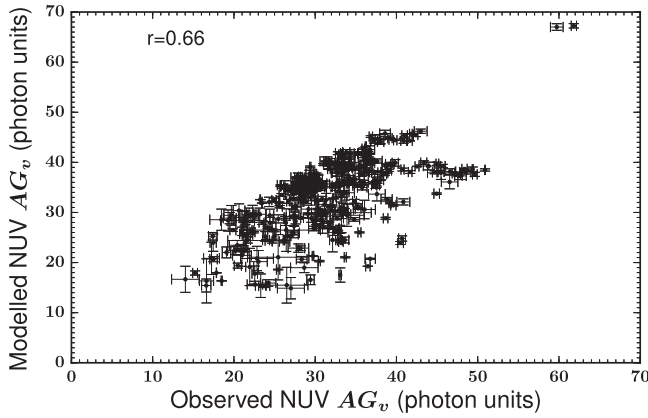


**Figure 9.** Correlation in the scatter plot between observed and modeled AG<sub>v</sub> in NUV.

respectively within a maximum error bar of  $\pm 40$  photon units. Correspondingly, we obtained the  $1\sigma$  error bars for the  $b$  model parameter in FUV and NUV as  $(1.23 \pm 0.1)$  and  $(1.18 \pm 0.09)$  respectively, which proves to be a clear indication of validation for the “baseline” airglow model obtained from the DIS observations (Narayanan et al. 2023). This gives us a practically applicable set of equations for FUV and NUV baseline airglow

$$\text{FUV: } AG_c = (1.23 \pm 0.1) \cdot \frac{\text{SF}}{\sin^3\left(\frac{\text{SA}}{2}\right)}, \quad (3)$$

$$\text{NUV: } AG_c = (1.18 \pm 0.09) \cdot \frac{\text{SF}}{\sin^3\left(\frac{\text{SA}}{2}\right)}. \quad (4)$$

From the results of the experiments conducted in this work, we noticed that the above model showed a remarkable degree

of compatibility with MIS data too, as evidenced by the high correlation between the observed and modeled baseline airglow values ( $AG_c$ ) for 311 NUV and 317 FUV MIS visits, shown in Figures 3 and 4.

## 2.2. Variable Airglow ( $AG_v$ )

We found the variable airglow component—which corresponds to area under the TEC bell curve—to have an inverse relation with SA as seen in Figure 5. We have represented the bell curves corresponding to the variation of TEC with time about local midnight by the equation  $\text{TEC} = C*(x)^2$  where  $C$  is the parabolic curvature and  $x$  is the hours from local midnight. We obtained this equation form for the “variable” airglow from the careful analysis of data conducted in Narayanan et al. (2023) that uncovered a parabolic relation between TEC and the local time during a single observation/visit’s duration. Having followed the same methodology we earlier used in the DIS observation experiments (Figures 6 and 7) to derive the relation between the parabola curvature  $C$  and SA—after avoiding bad (low exposure) data with observed variable airglow less than 20 photon units—we formulated the “variable” component of the airglow model.

As before, we again observed an inverse relation between  $C$  and SA at the date and time of observation. On checking if this relation is of the same nature as the SA dependency we observed in the “baseline” airglow  $AG_c$ , we observed that in both FUV and NUV observations,  $C$  is linearly correlated with  $\frac{1}{\sin^3(\text{SA}/2)}$  which is the Sun-angle-half of the solar expression we discussed earlier. Following the same procedure as in Narayanan et al. (2023), we obtained single expressions for  $C_{\text{FUV}}$  and  $C_{\text{NUV}}$  with respect to the SA quantity  $\frac{1}{\sin^3(\text{SA}/2)}$  (Figure 6, Figure 7).

In Figures 6 and 7, each plot point corresponds to a single observation/visit, and the error bar corresponds to the change in the curve-fit-obtained value for  $C$  when accommodating the extreme (with respect to the distance from the best-fit-curve) points of TEC values in a visit. Due to varying exposure times of different observations, this results in spread in  $AG_v$  caused by the extremal estimates of  $C$  accordingly changing from almost the same as the best-fit  $C$  to wildly different from it. We can mitigate this issue by weighing the plot points based on how “stable” the value of  $C$  is (i.e., minimal difference between the extremal  $C$  values), hence implicitly giving further importance to observations with longer exposure times (as a longer exposure time results in more gathered data and a longer parabolic curve, which lets us curve-fit with more accuracy). By doing so, we obtain a good linear correlation between the curve-fit  $C$  value and  $\frac{1}{\sin^3(\text{SA}/2)}$ . We use the slope and intercept hence obtained to define the expressions for  $C_{\text{FUV}}$  and  $C_{\text{NUV}}$  as

**Table 1**  
Observation Logs and Model Predictions for the Targets Under Study

Tile Name	<i>gl</i> (deg)	<i>gb</i> (deg)	NUV								FUV									
			Visits	<i>a</i>	<i>b</i>	Diffuse Radiation ± Error		Zodiacal Light		AG <sub>v</sub>	AG <sub>c</sub>	Total AG	Visits	<i>a</i>	<i>b</i>	Diffuse Radiation ± Error		AG <sub>v</sub>	AG <sub>c</sub>	Total AG
						(ph cm <sup>-2</sup> s <sup>-1</sup> sr <sup>-1</sup> Å <sup>-1</sup> )	(ph cm <sup>-2</sup> s <sup>-1</sup> sr <sup>-1</sup> Å <sup>-1</sup> )	(ph cm <sup>-2</sup> s <sup>-1</sup> sr <sup>-1</sup> Å <sup>-1</sup> )	(ph cm <sup>-2</sup> s <sup>-1</sup> sr <sup>-1</sup> Å <sup>-1</sup> )											
MIS2DFSGP_30767_0114	24.11	-51.21	2	625	1.36	1708 ± 13	881	38	202	240	2	561	1.35	762 ± 19	32	201	233			
MISDR1_03521_0440	170.29	33.72	4	901	1.63	1712 ± 15	644	38	167	205	2	858	0.50	905 ± 20	35	47	83			
MISDR1_03564_0550	172.94	38.72	2	674	1.53	1528 ± 12	652	39	201	240	2	562	0.50	628 ± 18	34	66	100			
MISDR1_03565_0549	172.65	37.76	2	801	1.53	1656 ± 13	655	39	201	240	2	564	0.50	630 ± 18	34	65	100			
MISDR1_03718_0548	175.31	35.47	2	894	0.50	1652 ± 16	694	38	64	102	2	476	1.68	692 ± 18	33	216	249			
MISDR1_03770_0548	176.52	35.64	2	776	0.50	1546 ± 12	706	37	64	101	2	599	0.50	663 ± 18	32	64	96			
MISDR1_04055_0432	178.57	27.01	1	1088	0.80	1970 ± 16	784	33	98	132	2	762	1.66	966 ± 22	25	205	230			
MISDR1_18032_0666	169.42	-65.57	2	695	0.77	1518 ± 12	729	37	94	132	2	534	0.50	595 ± 16	32	61	93			
MISDR1_18359_0454	179.91	-61.15	3	742	1.98	1697 ± 19	732	36	227	263	3	769	0.50	827 ± 21	32	57	89			
MISDR1_24292_0467	225.51	25.93	2	1071	1.28	1931 ± 14	759	37	101	138	1	1038	1.36	1151 ± 22	32	107	138			
MISDR1_24321_0468	227.98	27.77	2	962	1.41	1881 ± 13	736	38	183	221	1	788	0.99	917 ± 20	33	129	162			
MISDR1_26991_0464	196.78	-40.32	2	1504	2.44	2423 ± 14	680	33	250	284	3	2991	0.50	3043 ± 34	27	58	85			
MISDR1_26995_0462	193.40	-43.57	3	1200	1.64	2097 ± 14	697	37	200	237	2	1611	0.73	1675 ± 26	32	93	126			
MISDR1_28652_0417	113.56	-47.67	2	681	1.91	1695 ± 11	777	33	237	270	2	978	2.03	1233 ± 23	30	253	284			
MISDR1_28666_0417	114.14	-48.52	2	694	1.78	1695 ± 12	792	39	208	247	2	1022	1.94	1248 ± 22	35	226	262			
MISDR1_29116_0381	76.69	-53.73	3	684	0.74	1735 ± 12	974	29	77	107	3	760	1.48	913 ± 20	25	155	179			
MISDR1_29132_0390	106.66	-63.29	2	506	1.67	1523 ± 13	872	38	149	187	2	537	1.10	635 ± 17	33	98	131			
MISDR1_29134_0389	102.30	-62.73	2	589	0.89	1548 ± 11	877	38	82	120	2	591	1.39	719 ± 18	33	128	161			
MISDR1_29150_0381	75.21	-54.01	3	637	0.50	1657 ± 12	968	29	51	81	3	804	1.45	951 ± 21	25	148	173			
MISDR2_11565_0820	58.49	37.29	2	1056	0.50	1531 ± 14	376	67	99	166	2	720	0.50	819 ± 24	82	99	181			
MISDR2_15145_0888	192.82	21.17	3	1314	0.69	2324 ± 14	942	35	67	102	2	1136	0.50	1176 ± 22	31	40	71			
MISDR2_19739_0981	46.94	-23.53	5	1571	1.37	2503 ± 15	774	33	158	191	3	1546	1.78	1743 ± 28	27	202	229			
MISDR2_19776_0981	47.61	-24.39	4	1328	1.19	2244 ± 14	773	31	146	177	3	1362	1.57	1558 ± 25	24	198	223			
MISDR2_19777_0981	46.47	-24.33	4	1440	1.20	2377 ± 14	781	32	146	178	3	1322	1.53	1507 ± 26	25	187	211			
MISDR2_19814_0982	48.28	-25.25	2	1378	0.50	2229 ± 14	774	28	78	105	3	1394	1.40	1573 ± 25	23	180	203			
MISDR2_19815_0981	47.14	-25.20	4	1389	1.47	2330 ± 13	764	31	180	211	3	1381	1.41	1557 ± 25	27	178	205			
MISDR2_19854_0982	47.80	-26.08	5	1285	2.22	2325 ± 14	782	35	261	296	3	1392	1.49	1577 ± 25	28	187	215			
MISDR2_19894_0983	48.47	-26.95	3	1101	2.22	2200 ± 14	800	32	302	333	2	1426	0.50	1502 ± 24	26	76	102			
MISDR2_19922_0730	63.85	-26.83	3	1224	1.89	2138 ± 14	698	40	216	256	3	1346	1.90	1563 ± 27	41	217	258			
MISDR2_20006_0731	66.41	-28.20	3	1215	1.77	2125 ± 13	699	44	210	254	3	1832	0.50	1893 ± 27	46	60	106			
MISDR2_20007_0731	65.29	-28.38	3	1143	1.82	2062 ± 14	708	41	211	252	3	1297	2.03	1525 ± 25	43	235	278			
MISDR2_20050_0732	67.15	-28.96	3	1242	0.50	2006 ± 13	704	46	60	106	3	1524	1.75	1735 ± 27	49	211	260			
MISDR2_20052_0731	64.90	-29.32	4	1000	1.93	1943 ± 12	722	39	224	263	4	1148	1.90	1365 ± 23	41	221	262			
MISDR2_20109_0986	51.77	-31.29	1	1228	0.79	1985 ± 12	696	40	62	102	3	1198	1.42	1366 ± 24	30	170	200			
MISDR2_20155_0986	52.43	-32.15	2	1227	0.50	2136 ± 13	839	31	71	102	2	1265	0.50	1336 ± 23	26	71	97			
MISDR2_20399_0990	57.09	-36.32	2	874	1.61	1832 ± 12	814	37	148	185	2	927	1.40	1056 ± 21	31	129	160			
MISDR2_20402_0989	53.38	-36.53	1	1031	0.86	1858 ± 12	762	38	65	103	3	873	1.27	1020 ± 22	28	147	175			
MISDR2_20454_0990	54.12	-37.37	2	988	0.50	1906 ± 13	864	33	54	87	2	971	1.45	1092 ± 23	27	121	148			
MISDR2_20505_0371	57.37	-38.06	1	870	1.42	1904 ± 13	874	36	160	195	2	1323	1.17	1432 ± 24	31	109	141			
MISDR2_21102_0717	49.66	-47.25	3	701	1.53	1963 ± 12	1055	28	207	235	3	769	2.01	1045 ± 21	23	272	295			
MISDR2_21199_0744	91.77	-41.92	3	920	0.50	1722 ± 13	749	36	53	89	2	717	2.22	926 ± 20	32	208	240			
MISDR2_21200_0744	90.67	-42.36	3	840	0.50	1650 ± 12	757	37	53	90	2	745	2.16	948 ± 19	32	203	235			
MISDR2_21350_0379	72.24	-49.50	2	633	1.30	1602 ± 12	860	38	109	147	2	1064	1.21	1165 ± 22	33	101	134			
MISDR2_21351_0378	70.94	-49.72	2	700	0.50	1636 ± 12	894	38	43	81	2	1164	1.45	1288 ± 23	33	125	158			
MISDR2_24267_0504	244.07	47.62	10	567	2.13	1641 ± 12	928	31	149	180	7	710	1.79	833 ± 20	24	127	151			
MISDR2_26174_0577	242.88	50.69	2	489	2.05	1611 ± 12	982	34	142	176	1	658	0.98	726 ± 17	29	68	97			
MISDR2_29119_0379	73.09	-51.39	2	656	1.39	1647 ± 12	870	38	122	160	2	942	1.03	1032 ± 21	33	90	123			
MISDR3_20300_0988	53.25	-34.77	3	908	0.50	1816 ± 12	867	30	42	72	3	807	1.93	967 ± 20	23	153	176			
MISDR3_20350_0988	53.92	-35.63	3	1465	0.50	2380 ± 12	873	28	43	71	2	1334	2.44	1536 ± 25	25	203	228			
MISGCSAN_04679_0860	190.36	28.08	3	1054	0.50	1999 ± 12	912	26	35	60	3	708	1.63	817 ± 20	21	113	134			

**Table 1**  
(Continued)

Tile Name	<i>gl</i> (deg)	<i>gb</i> (deg)	NUV									FUV								
			Visits	<i>a</i>	<i>b</i>	Diffuse Radiation ± Error		Zodiacal Light (ph cm <sup>-2</sup> s <sup>-1</sup> sr <sup>-1</sup> Å <sup>-1</sup> )	AG <sub>v</sub>	AG <sub>c</sub>	Total AG	Visits	<i>a</i>	<i>b</i>	Diffuse Radiation ± Error		AG <sub>v</sub>	AG <sub>c</sub>	Total AG	
MISGCSAN_15725_1923	205.02	24.00	2	1152	0.50	2198 ± 14	1012	35	35	69	2	1179	0.50	1214 ± 23	28	35	63			
MISGCSAN_15879_1930	198.74	34.66	2	1018	0.50	2011 ± 13	960	36	34	69	2	784	1.96	916 ± 19	30	132	161			
MISGCSAN_15935_1932	198.43	36.17	2	788	0.50	1765 ± 13	943	36	34	70	2	679	1.52	781 ± 21	30	102	132			
MISGCSAN_15938_1930	200.86	34.20	2	687	1.82	1797 ± 12	987	36	123	159	2	607	1.51	709 ± 17	29	102	131			
MISGCSAN_15939_1929	201.63	33.52	2	751	1.85	1876 ± 12	1001	36	124	160	2	846	0.50	880 ± 19	29	34	63			
MISGCSN_17639_0402o	154.72	-57.66	1	548	0.77	1524 ± 12	924	35	52	88	2	525	0.50	559 ± 15	25	34	60			
MISGCSN_17683_0404o	156.59	-56.96	2	534	1.46	1551 ± 14	917	35	101	136	2	510	0.50	545 ± 15	29	35	64			
MISGCSN_17776_0404o	159.60	-57.83	2	624	1.63	1626 ± 17	888	35	114	150	2	484	1.46	586 ± 16	29	102	131			
MISGCSN_18126_0407o	169.22	-54.01	2	836	0.50	1692 ± 15	820	36	36	72	2	879	0.50	915 ± 19	30	36	66			
MISGCSN_19978_0983o	48.66	-28.52	1	1308	1.11	2120 ± 13	731	35	81	116	1	1404	0.74	1458 ± 23	31	54	85			
MISGCSN_21091_0376o	64.23	-46.75	2	1037	0.50	1897 ± 16	824	36	37	73	2	1436	0.50	1472 ± 25	32	37	69			
MISGCSN_29112_0383o	82.00	-56.35	1	650	0.85	1574 ± 12	853	44	72	116	3	757	1.35	864 ± 20	37	107	145			
MISGCSN_29147_0383o	79.12	-56.16	3	534	1.60	1523 ± 12	864	29	127	156	3	654	1.56	776 ± 20	27	124	150			
MISGCSS_17640_0402	154.58	-58.43	2	523	1.44	1537 ± 11	914	35	101	136	2	549	0.50	584 ± 15	29	35	64			
MISGCSS_17641_0402	154.41	-59.43	2	551	0.50	1488 ± 12	902	35	35	70	2	552	0.50	587 ± 15	29	35	64			
MISGCSS_17731_0403	157.82	-59.38	2	547	1.49	1532 ± 11	884	35	102	137	2	538	0.50	572 ± 15	29	34	63			
MISGCSS_17774_0702	159.56	-55.85	2	624	0.50	1564 ± 12	905	35	35	70	2	784	0.50	819 ± 18	29	35	64			
MISGCSS_17775_0404o	159.57	-56.84	2	578	0.50	1508 ± 11	896	35	34	69	2	548	0.50	582 ± 15	29	34	63			
MISGCSS_17777_0404o	159.55	-58.83	2	610	0.50	1524 ± 11	880	35	35	71	2	524	0.50	559 ± 15	29	35	65			
MISGCSS_17871_0405	162.76	-56.71	2	564	0.50	1475 ± 11	877	36	35	71	2	498	1.45	599 ± 16	30	101	131			
MISGCSS_17918_0406	164.01	-54.16	3	617	0.50	1545 ± 11	893	30	36	66	3	651	1.80	779 ± 17	26	128	155			
MISGCSS_18071_0406o	167.40	-52.61	2	927	0.51	1850 ± 13	880	28	44	72	2	929	1.32	1043 ± 21	28	113	141			
MISGCSS_18347_0409	174.50	-49.85	1	710	0.50	1592 ± 11	841	45	43	88	2	1201	0.50	1243 ± 23	40	43	82			
MISGCSS_18348_0410	174.80	-50.83	2	824	0.50	1700 ± 13	832	32	44	76	2	1196	0.50	1240 ± 23	32	44	76			
MISGCSS_18466_0410	177.58	-50.25	3	981	0.50	1703 ± 12	683	40	42	82	3	1133	0.50	1174 ± 22	39	42	82			
MISGCSS_18524_0410	177.97	-47.71	2	870	0.50	1738 ± 13	826	43	42	85	2	1309	1.22	1410 ± 24	41	102	143			
MISGCSS_18647_0410	180.21	-46.24	1	1079	0.76	1958 ± 13	816	42	64	106	1	1524	0.78	1590 ± 25	42	65	108			
MISGCSS_18710_0410	181.30	-45.50	2	993	1.28	1904 ± 13	810	42	101	143	2	1589	0.50	1629 ± 26	39	40	79			
MISGCSS_18772_0410	181.61	-43.05	2	1000	0.50	1861 ± 13	822	41	39	80	2	1618	1.32	1720 ± 26	38	102	141			
MISGCSS_18775_0410	182.79	-45.61	2	1006	0.50	1842 ± 13	796	42	40	82	2	1280	1.27	1383 ± 25	40	103	143			
MISGCSS_18840_0410o	183.58	-45.10	2	1021	0.50	1719 ± 14	659	42	39	81	2	1184	1.38	1292 ± 24	39	108	147			
MISGCSS_26706_0416	186.74	-39.30	2	1254	1.42	2153 ± 13	794	39	106	145	2	2272	1.45	2380 ± 31	35	108	143			
MISGCSS_26737_0416o	189.00	-38.47	2	1717	0.50	2413 ± 13	657	40	39	79	2	3207	0.50	3246 ± 37	36	39	75			
MISGCSS_26738_0416o	188.11	-39.34	2	1492	0.50	2189 ± 14	659	40	38	78	2	2787	1.45	2896 ± 37	37	109	146			
MISGCSS_26770_0416o	189.80	-38.58	2	1732	0.50	2421 ± 14	651	40	38	78	2	3184	1.52	3301 ± 37	37	116	153			
MISGCSS_29051_0679	79.60	-53.11	2	777	0.50	1734 ± 13	922	36	36	72	2	852	1.53	960 ± 21	31	109	139			
MISWZN09_24357_0202	226.47	24.33	2	1048	0.50	1870 ± 13	788	37	35	72	2	928	1.59	1039 ± 23	31	111	142			
MISWZN09_24389_0202	228.28	25.26	2	838	1.72	1737 ± 13	778	37	122	159	2	669	1.42	769 ± 18	32	101	132			
MISWZN09_24391_0202	226.94	23.53	2	1034	0.50	1845 ± 13	776	37	35	72	2	788	1.45	890 ± 19	31	102	134			
MISWZS00_29045_0150	88.54	-56.81	3	606	0.50	1651 ± 11	1012	29	35	64	3	678	0.50	712 ± 17	24	35	59			
MISWZS00_29046_0150	86.92	-56.27	2	445	1.66	1563 ± 12	1003	36	115	151	2	621	1.54	728 ± 17	29	107	136			
MISWZS00_29073_0165	93.87	-59.23	1	673	0.53	1631 ± 11	922	35	37	72	3	715	1.86	865 ± 21	34	153	186			
MISWZS00_29077_0150	86.97	-57.27	2	456	1.57	1584 ± 11	1019	35	109	144	2	609	1.64	722 ± 17	29	114	142			
MISWZS00_29078_0150	85.37	-56.70	1	551	0.58	1556 ± 11	966	35	40	75	3	605	1.58	714 ± 19	24	112	136			
MISWZS00_29105_0165	94.07	-60.21	2	679	0.50	1577 ± 12	855	42	43	85	2	486	2.42	696 ± 17	40	210	250			
MISWZS00_29106_0165	92.23	-59.77	3	398	2.50	1531 ± 12	920	36	216	252	3	470	2.50	685 ± 17	34	216	251			
MISWZS00_29110_0165	85.36	-57.70	2	480	1.60	1626 ± 12	1035	35	112	147	2	633	1.53	740 ± 17	29	107	136			
MISWZS00_29141_0165	88.75	-59.79	2	457	1.54	1606 ± 11	1043	36	107	142	2	603	0.50	638 ± 16	29	35	64			
MISWZS00_29143_0165	85.34	-58.70	2	583	1.64	1743 ± 12	1045	35	115	150	2	586	1.60	698 ± 17	29	112	141			
MISWZS00_29144_0165	83.63	-58.10	7	751	2.25	1837 ± 14	915	25	174	199	7	919	0.50	958 ± 22	24	39	63			

**Table 1**  
(Continued)

Tile Name	<i>gl</i> (deg)	<i>gb</i> (deg)	NUV								FUV								
			Visits	<i>a</i>	<i>b</i>	Diffuse Radiation ± Error		Zodiacal Light	AG <sub>v</sub>	AG <sub>c</sub>	Total AG	Visits	<i>a</i>	<i>b</i>	Diffuse Radiation ± Error		AG <sub>v</sub>	AG <sub>c</sub>	Total AG
						( ph cm <sup>-2</sup> s <sup>-1</sup> sr <sup>-1</sup> Å <sup>-1</sup> )	( ph cm <sup>-2</sup> s <sup>-1</sup> sr <sup>-1</sup> Å <sup>-1</sup> )								( ph cm <sup>-2</sup> s <sup>-1</sup> sr <sup>-1</sup> Å <sup>-1</sup> )				
MISWZS00_29409_0164	72.67	-61.10	1	471	0.94	1584 ± 11	1043	36	71	107	1	593	0.52	632 ± 16	30	39	69		
MISWZS01_17396_0267	143.86	-60.22	3	523	2.42	1628 ± 17	939	32	168	200	3	499	1.62	611 ± 16	27	112	139		
MISWZS01_17514_0267	149.17	-59.90	2	514	0.93	1470 ± 11	884	36	73	108	2	606	0.79	668 ± 17	30	62	92		
MISWZS01_17556_0267	150.71	-60.43	3	370	2.44	1430 ± 12	895	34	169	203	3	478	1.62	590 ± 16	28	112	140		
MISWZS01_29029_0266	120.03	-61.47	2	471	0.50	1390 ± 11	884	37	36	73	2	443	0.82	502 ± 15	32	58	90		
MISWZS01_29031_0266	115.59	-61.41	2	532	1.45	1531 ± 11	896	37	103	140	2	474	0.50	509 ± 15	32	35	67		
MISWZS01_29033_0288	111.23	-61.17	3	492	0.50	1527 ± 12	1001	35	34	68	3	529	0.50	563 ± 15	28	34	62		
MISWZS01_29060_0266	120.99	-62.27	3	545	1.70	1584 ± 14	919	35	120	155	3	401	1.54	509 ± 19	30	108	138		
MISWZS01_29063_0266	114.19	-62.18	2	429	0.57	1486 ± 11	1017	34	42	76	2	418	1.52	531 ± 15	29	113	142		
MISWZS01_29064_0268	111.96	-62.05	3	421	1.69	1548 ± 12	1010	34	119	152	3	580	0.50	616 ± 16	28	35	63		
MISWZS01_29097_0268	110.47	-62.79	3	543	0.50	1573 ± 12	997	35	33	69	3	408	1.52	510 ± 15	29	102	131		
MISWZS01_29123_0266	127.82	-63.56	2	530	1.45	1613 ± 12	981	33	102	135	2	620	1.56	730 ± 19	28	109	137		
MISWZS01_29124_0266	125.45	-63.73	3	453	1.92	1519 ± 11	932	34	134	167	3	538	1.62	651 ± 16	28	112	141		
MISWZS03_18855_0284	192.18	-57.40	1	582	0.94	1297 ± 12	644	38	71	109	1	541	0.61	587 ± 17	34	46	80		
MISWZS03_27657_0283	206.04	-52.65	2	860	0.50	1494 ± 12	587	40	48	88	2	722	2.14	926 ± 19	37	203	240		
MISWZS03_27658_0283	205.16	-53.44	2	775	0.50	1419 ± 12	593	40	51	91	2	747	0.50	798 ± 18	37	51	88		
MISWZS03_27712_0283	206.98	-53.45	2	840	0.50	1471 ± 11	582	40	48	89	2	641	2.08	842 ± 19	37	201	238		
MISWZS03_27713_0283	206.10	-54.24	2	629	2.04	1419 ± 12	590	40	201	241	2	746	0.50	795 ± 20	37	49	86		
MISWZS22_20249_0162	54.96	-33.83	4	1080	0.69	1944 ± 14	810	26	53	78	4	1004	0.52	1040 ± 22	22	40	61		
MISWZS22_20349_0162	55.08	-35.54	3	899	1.72	1887 ± 13	860	26	128	153	3	1035	1.47	1145 ± 22	22	109	131		
MISWZS22_20351_0261	52.71	-35.66	2	1457	1.99	2467 ± 16	863	35	149	184	2	1414	1.51	1527 ± 25	29	113	142		
MISWZS22_20400_0261	55.86	-36.40	1	916	1.16	1857 ± 13	861	24	81	105	3	1092	0.54	1131 ± 23	20	42	62		
MISWZS22_20403_0261	52.16	-36.56	3	957	0.50	1780 ± 12	780	36	39	75	3	826	1.39	935 ± 22	33	109	142		
MISWZS22_20448_0157	61.53	-36.80	4	929	0.56	1716 ± 12	737	38	44	82	4	1146	0.50	1186 ± 22	33	40	73		
MISWZS22_20558_0157	59.40	-38.79	3	742	1.34	1719 ± 12	875	27	101	128	3	1000	0.50	1039 ± 21	23	38	60		
MISWZS22_20669_0157	61.00	-40.44	3	807	0.50	1731 ± 12	887	31	38	70	3	938	0.50	976 ± 19	26	38	64		
MISWZS22_20671_0261	58.42	-40.62	3	737	2.11	1798 ± 13	906	25	160	185	3	1001	1.90	1142 ± 22	21	143	164		
MISWZS22_20672_0261	57.15	-40.70	2	960	0.50	1884 ± 15	886	26	37	63	2	1449	1.94	1588 ± 25	23	143	165		
MISWZS22_20202_0162	53.05	-32.98	3	1253	0.50	2129 ± 14	839	25	37	62	...	...	...	...	...	...	...		
MISDR2_19977_0984	49.79	-28.69	...	...	...	...	...	...	...	...	2	1205	1.41	1413 ± 24	25	207	233		
MIS2DFSGP_40462_0246	19.11	-47.96	...	...	...	...	...	...	...	...	1	764	0.50	858 ± 19	35	55	90		
MISGCSN_21218_0378o	69.04	-47.88	...	...	...	...	...	...	...	...	3	1046	1.53	1157 ± 23	23	112	135		
MISGCSS_18711_0410	181.70	-46.37	...	...	...	...	...	...	...	...	2	1381	0.50	1421 ± 24	40	40	80		
MISGCSS_18774_0410	182.38	-44.76	...	...	...	...	...	...	...	...	2	1438	0.50	1478 ± 26	39	40	79		
MISDR2_29151_0380	73.99	-53.23	...	...	...	...	...	...	...	...	2	858	0.65	916 ± 22	24	58	82		

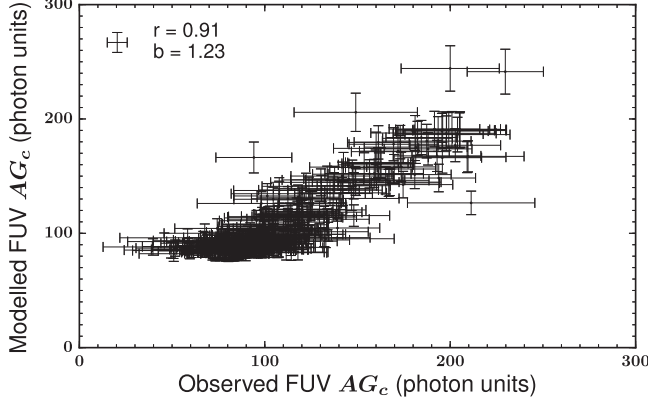


**Figure 10.** Correlation plot of observed and modeled  $AG_c$  with fixed scaling factor  $b = 1.23$  in FUV.

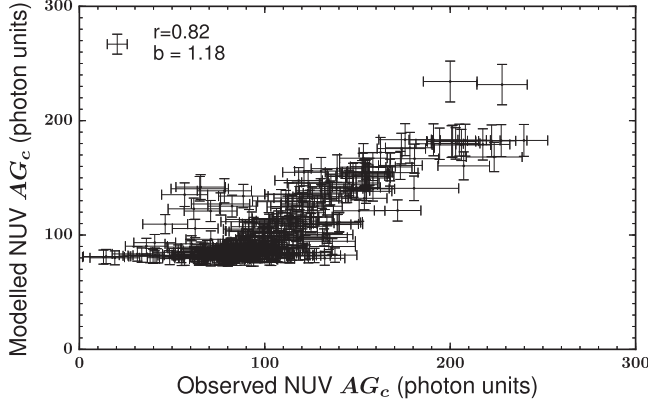


**Figure 11.** Correlation plot of observed and modeled  $AG_c$  with fixed scaling factor  $b = 1.18$  in NUV.

follows

$$C_{\text{FUV}} = \left[ \frac{10.05}{\sin^3\left(\frac{\text{SA}}{2}\right)} - 3.8 \right].$$

$$C_{\text{NUV}} = \left[ \frac{6.47}{\sin^3\left(\frac{\text{SA}}{2}\right)} + 0.67 \right].$$

The discontinuity found in the scatter plot between the calculated variable airglow and the SA in Figure 5 is due to the sparseness of MIS observations in the SA range  $[100^\circ, 120^\circ]$ . The error bars for curvature  $C$  correspond to the change in the parabolic curvature  $C$  on fitting quadratics to the extreme data points. By taking the area under the “TEC versus hours from local midnight” curve, we obtain the following modeling

equations for the “variable” airglow in UV visits.

FUV:  $AG_v$

$$= \left[ \frac{10.05}{\sin^3\left(\frac{\text{SA}}{2}\right)} - 3.8 \right] * 0.00296 * \text{Exposure Time (in s)}, \quad (5)$$

NUV:  $AG_v$

$$= \left[ \frac{6.47}{\sin^3\left(\frac{\text{SA}}{2}\right)} + 0.67 \right] * 0.00296 * \text{Exposure Time (in s)}. \quad (6)$$

The variable part of airglow ( $AG_v$ ) corresponding to the average area under the curve is proportional to the product of curvature ( $C$ ) and the exposure time of each visit. We can observe the correlation between observed and modeled  $AG_v$  of medium observations in FUV and NUV in Figures 8 and 9 respectively. We have tabulated the observation logs and the modeled airglow values ( $AG_c$  and  $AG_v$ ) of 136 FUV and 137 NUV MIS observations in Table 1.

### 3. Discussion and Conclusion

The AIS, MIS and DIS observations by the GALEX telescope (hosted in the GALEX MAST Archive) have been instrumental for UV research in recent years. Most recently, in Narayanan et al. (2023), we modeled and calculated foreground emissions in DIS FUV and NUV observations with remarkable accuracy. Using mathematical and machine learning techniques like Huber-loss-augmented Robust Regression (Huber 1964) and K-Fold Cross Validation, we were able to identify an outlier-resilient and generalizable empirical model form that best captures the dependencies between airglow, TECMIN, SA and SF. Through the chi-square minimization technique, we were able to further set a singular value for the parameter “ $b$ ” in the  $AG_c$  model at 1.25 and 1.18 in FUV and NUV respectively. We used these models to successfully predict and extract foreground emissions in DIS observation tiles.

We adopted the same methodology in this work to independently arrive at an airglow model for MIS data to check two things. First, we wanted to verify if the same framework and approach we put forth for DIS are adaptable and general enough to be applied on MIS with good accuracy. Second, if the former objective is accomplished, then the MIS and DIS models are concordant. We use the term “concordant” here to indicate whether the new model lies within the permissible error margins of the old model.

We obtained an excellent correlation between the observed and modeled “baseline” and “variable” airglow in both FUV and NUV observations, as seen in Figures 3, 4, 8 and 9. Here, the  $b$  parameter in  $AG_c$  model has been fixed to 1.23 and 1.18 in FUV and NUV observations respectively, using chi-square minimization by varying  $b$  values in the range  $[0.5, 2.5]$  with a step size of 0.01.

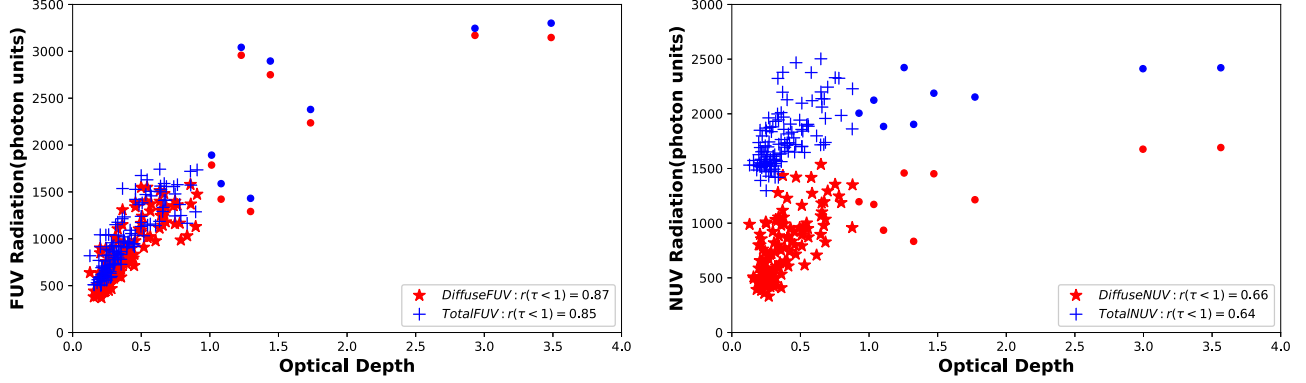


**Figure 12.** FUV (left) and NUV (right) total radiation (+) and foreground subtracted background radiation (\*) are plotted against the optical depth. Solid circles represent the observations with optical depth  $>1$  where the saturation of UV emissions is clearly visible. Correlation coefficients in the low density region ( $\tau < 1$ ) are provided in the legend.

The fixed values had the lowest reduced chi-square of 0.3 and 0.1, within an error margin of  $\pm 40$  photon units (Sujatha et al. 2009). Even after fixing the scaling factor  $b$  in the “baseline” model, we still observed a significant correlation between the modeled  $AG_c$  and observed  $AG_c$  in both FUV and NUV within  $1\sigma$  error bars (Figures 10 and 11 respectively). We also observed that the total, as well as the foreground subtracted diffuse background in regions with  $\tau < 1$ , are reasonably well correlated with the optical depth of the region both in FUV and NUV, which indicates that the dominant contributor of the diffuse UV emission in the sky is the starlight scattered from interstellar dust grains (Figure 12). Our analysis shows that the total foreground emission varies between 59 and 295 photon units in FUV whereas in NUV, it varies between 671 and 1195 photon units depending upon the date and time of observation. The decrease in the correlation seen in the NUV might be due to the error in the estimation of zodiacal light which is one of the dominant contributors of the foreground emission in NUV band. This is the subject of further investigations we are pursuing to improve the zodiacal light model using more NUV GALEX observations.

### Acknowledgments

This research is based on data from NASA’s GALEX program. Data presented in this paper were obtained from the Mikulski Archive for Space Telescopes (MAST). STScI is operated by the Association of Universities for Research in Astronomy, Inc., under NASA contract NAS5-26555. Support

for MAST for non-HST data is provided by the NASA Office of Space Science via grant NNX09AF08G and by other grants and contracts. S.N.V. acknowledges the support of DST-FIST. Programming languages GDL and Python were used for the data analysis.

Facility: GALEX.

### ORCID iDs

Shivashankar S. Menon <https://orcid.org/0000-0001-7009-272X>  
N. V. Sujatha <https://orcid.org/0000-0001-6787-6080>

### References

- Boffi, F. R., Biretta, J., Bohlin, R., et al. 2007, ACS Instrument Handbook, Version 8.0 (Baltimore: STScI)
- Bowyer, S. 1991, *ARA&A*, **29**, 59
- Chatterjee, T. N., & Das, T. K. 1995, *MNRAS*, **274**, 858
- Henry, R. C. 1991, *ARA&A*, **29**, 89
- Huber, P. J. 1964, *Ann. Math. Stat.*, **35**, 73
- Leinert, C., Bowyer, S., Haikala, L. K., et al. 1998, *A&AS*, **127**, 1
- Martin, D. C., Fanson, J., Schiminovich, D., et al. 2005, *ApJL*, **619**, L1
- Morrissey, P., Conrow, T., Barlow, T. A., et al. 2007, *ApJS*, **173**, 682
- Murthy, J. 2009, *Ap&SS*, **320**, 21
- Murthy, J. 2014a, *ApJS*, **213**, 32
- Murthy, J. 2014b, *Ap&SS*, **349**, 165
- Narayanan, N., Menon, S. S., & Sujatha, N. V. 2023, *AdSpR*, **71**, 1059
- Sujatha, N. V., Murthy, J., Karnataki, A., Henry, R. C., & Bianchi, L. 2009, *ApJ*, **692**, 1333
- Sujatha, N. V., Murthy, J., Suresh, R., Henry, R. C., & Bianchi, L. 2010, *ApJ*, **723**, 1549